International Journal of Applied Earth Observation and Geoinformation 148 (2026) 105229

Contents lists available at ScienceDirect

International Journal of Applied Earth Observation and Geoinformation

journal homepage: www.elsevier.com/locate/jag

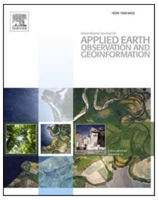

Contrasting trends in climatic and ecohydrological aridity over one-fifth of global drylands

Lei He[a,b,c], Alexis Berg[d], Kailiang Yu[e], Jian-Sheng Ye[f], Josep Peñuelas[g,h], Philippe Ciais[i], Jingfeng Xiao[j], Xu Lian[k], Jianping Huang[l], Jing Li[a], Wei Li[m], Jian Peng[n], Songhan Wang[o], Ning Ma[p], Zecheng Guo[c], Thomas W. Crowther[q], Jiangpeng Cui[r], Chenghu Zhou[s], Yaowen Xie[c,t,u,*], Zhao-Liang Li[a,v,**]

[a] *State Key Laboratory of Efficient Utilization of Arable Land in China, Institute of Agricultural Resources and Regional Planning, Chinese Academy of Agricultural Sciences, Beijing 100081, China*
[b] *National Tibetan Plateau Data Center, State Key Laboratory of Tibetan Plateau Earth System, Environment and Resources, Institute of Tibetan Plateau Research, Chinese Academy of Sciences, Beijing 100101, China*
[c] *College of Earth and Environment Sciences, Lanzhou University, Lanzhou 730000, China*
[d] *Department of Geography, Université de Montréal, Montréal, QC H2V 0B3, Canada*
[e] *Department of Ecology & Evolutionary Biology, Princeton University, Princeton, NJ 08544, USA*
[f] *State Key Laboratory of Grassland Agro-ecosystems, College of Ecology, Lanzhou University, Lanzhou 730000, China*
[g] *CSIC, Global Ecology CREAF-CSIC-UAB, Cerdanyola del Vallès, 08193 Barcelona, Catalonia, Spain*
[h] *CREAF, Cerdanyola del Vallès, 08193 Barcelona, Catalonia, Spain*
[i] *Laboratoire des Sciences du Climat et de l'Environnement, CEA/CNRS/UVSQ/Université Paris Saclay, Gif-sur-Yvette 91191, France*
[j] *Earth Systems Research Center, Institute for the Study of Earth, Oceans, and Space, University of New Hampshire, Durham, NH 03824, USA*
[k] *Department of Earth and Environmental Engineering, Columbia University, New York, NY 10027, USA*
[l] *Key Laboratory for Semi-Arid Climate Change of the Ministry of Education, College of Atmospheric Sciences, Lanzhou University, Lanzhou 730000, China*
[m] *Department of Earth System Science, Ministry of Education Key Laboratory for Earth System Modeling, Institute for Global Change Studies, Tsinghua University, Beijing, China*
[n] *Department of Remote Sensing, Helmholtz Centre for Environmental Research-UFZ, Permoserstrasse 15, 04318 Leipzig, Germany*
[o] *Jiangsu Collaborative Innovation Center for Modern Crop Production/Key Laboratory of Crop Physiology and Ecology in Southern China, College of Agriculture, Nanjing Agricultural University, Nanjing 210095, China*
[p] *Key Laboratory of Water Cycle and Related Land Surface Processes, Institute of Geographic Sciences and Natural Resources Research, Chinese Academy of Sciences, Beijing 100101, China*
[q] *Institute of Integrative Biology, ETH Zurich (Swiss Federal Institute of Technology), 8092 Zurich, Switzerland*
[r] *State Key Laboratory of Tibetan Plateau Earth System, Environment and Resources (TPESER), Institute of Tibetan Plateau Research, Chinese Academy of Sciences, Beijing 100101, China*
[s] *Center for Ocean Remote Sensing of Southern Marine Science and Engineering Guangdong Laboratory (Guangzhou), Guangzhou Institute of Geography, Guangdong Academy of Sciences, Guangzhou 510070, China*
[t] *Key Laboratory of Western China's Environmental Systems (Ministry of Education), Lanzhou University, Lanzhou 730000, China*
[u] *The Data Intelligence Laboratory of Tibetan Plateau Humanistic Environment, Lanzhou University, Lanzhou 730000, China*
[v] *State Key Laboratory of Resources and Environmental Information System, Institute of Geographic Sciences and Natural Resources Research, Chinese Academy of Sciences, Beijing 100101, China*

ARTICLE INFO

Keywords:
Dryland
Ecohydrological aridity
Climatic aridity
eCO$_2$-induced effects

ABSTRACT

Climatic aridity interplays with ecohydrological aridity, generally showing synchronous increasing trends under global warming. However, these changes can be decoupled and even exhibit contrasting temporal variations. The spatial patterns and underlying mechanisms of such contrasting aridity changes remain poorly understood. Utilizing satellite and climate data, we demonstrate that nearly one-fifth (22.3%) of global vegetated drylands showed contrasting trends in climatic and ecohydrological aridity over the past four decades. Approximately 60% of these areas experienced an increase in climatic aridity but a decrease in ecohydrological aridity, while

---

* Corresponding author at: College of Earth and Environment Sciences, Lanzhou University, Lanzhou 730000, China.
** Corresponding author at: State Key Laboratory of Efficient Utilization of Arable Land in China, Institute of Agricultural Resources and Regional Planning, Chinese Academy of Agricultural Sciences, Beijing 100081, China.
E-mail addresses: xieyw@lzu.edu.cn (Y. Xie), lizhaoliang@caas.cn (Z.-L. Li).

https://doi.org/10.1016/j.jag.2026.105229
Received 26 June 2025; Received in revised form 12 February 2026; Accepted 4 March 2026

others exhibited opposite temporal trends. These divergences stem primarily from elevated atmospheric CO_2 levels, which exert opposite effects on ecohydrological aridity via vegetation structure and canopy stomatal conductance. These findings highlight the nonlinear nature of vegetation-climate interactions in drylands and provide new insight into water and carbon cycling in global drylands under climate change.

1. Introduction

Global warming drives complex shifts in surface climate and moisture regimes across the globe (Zaitchik et al., 2023; Koppa et al., 2024). Yet, projections of future terrestrial moisture conditions remain highly uncertain, with some models forecasting widespread land drying (Scheff and Frierson, 2014; Cook et al., 2014; Sherwood and Fu, 2014), while others project changes in line with current patterns, with more precipitation in wet regions and less in arid regions (Seager et al., 2010; Chou et al., 2009; Held and Soden, 2006). Beyond climatic aridity, considerable uncertainty remains regarding ecohydrological aridity, which describes the extent to which moisture availability constrains vegetation growth (Slette et al., 2019; Cui et al., 2024). Notably, ecohydrological aridity can become substantially decoupled from climatic aridity under certain conditions (Song et al., 2022; Miller et al., 2023; Lian et al., 2021). The spatial patterns and underlying drivers of this decoupling remain poorly understood, potentially biasing assessments of climate change impacts and land–atmosphere feedbacks.

Assessments of aridity changes in drylands reveal contrasting patterns when interpreted from climatic versus ecological perspectives (Lian et al., 2021). Projections of future dryland extent diverge depending on the aridity index applied: the climatic aridity index (AI, the ratio of annual precipitation to potential evapotranspiration, where lower values indicate drier conditions) suggests accelerated expansion (Huang et al., 2016), whereas the ecohydrological aridity index (EI, where lower values indicate higher ecohydrological aridity; see Methods), which incorporates vegetation responses to elevated atmospheric CO_2 concentration (eCO_2), implies minimal or no change (Berg and McColl, 2021). Furthermore, satellite observations show a pronounced increase in vegetation greenness across drylands in recent decades, despite a concurrent intensification of climatic aridity (Donohue et al., 2013; Gonsamo et al., 2021). These findings point to a decoupled pattern of increased climatic aridity but decreased ecohydrological aridity (AI↓ & EI↑), which can be attributed to enhanced ecosystem water use efficiency (WUE) driven by eCO_2 (Gonsamo et al., 2021). Understanding the mechanisms underlying this decoupling is critical for predicting which ecosystems may remain resilient in a warmer and potentially drier future. However, despite growing recognition of this phenomenon, its spatial distribution remains poorly constrained, largely due to challenges in monitoring ecohydrological aridity at large scales (Cui et al., 2024). Moreover, an opposite mode of contrast, characterized by decreased climatic aridity but increased ecohydrological aridity (AI↑ & EI↓), has received far less attention, even though climate-driven shifts in vegetation composition and dynamics can intensify ecohydrological stress (Zhu et al., 2016; Jump et al., 2017; Chai et al., 2025). Although such contrasting climatic and ecohydrological aridity changes are expected to strongly affect ecosystem functioning and biogeochemical cycling under ongoing climate change, their spatial patterns and underlying mechanisms across global drylands remain largely unexplored.

To address these outstanding uncertainties, we ask two questions: (1) how are the two types of contrasting climatic and ecohydrological aridity changes (i.e., AI↓ & EI↑ and AI↑ & EI↓) distributed across global drylands in recent decades? And (2) what mechanisms underlie these contrasting patterns? To answer these questions, we analyzed recent trends in both climatic and ecohydrological aridity across global drylands during 1982–2018. We employed a recently developed EI, which integrates vegetation condition (leaf area index, LAI) and soil moisture (SM) limitation, quantified as the correlation between SM and vegetation transpiration (Tran) [cor(SM,Tran)] (see Methods). Our analysis reveals the spatial distribution and underlying drivers of decoupled climatic and ecohydrological aridity changes, offering new insights into the water and carbon cycle dynamics of global drylands under climate change.

2. Methods

2.1. Climatic and ecohydrological aridity

We utilized a widely used measure of climatic aridity, aridity index (AI) (Huang et al., 2016; Dai et al., 2018), defined as

$$\mathrm{AI} = \mathrm{P} / \mathrm{PET} \tag{1}$$

where P denotes annual precipitation, and PET represents annual potential evapotranspiration.

Current monitoring and assessment of ecohydrological aridity changes remain challenging (Cui et al., 2024). While LAI has been used to indicate ecological aridity, it primarily reflects the vegetation growth state rather than water availability limitations on vegetation (Shi et al., 2023). To estimate the trend of ecohydrological aridity, a newly developed ecohydrological aridity index (EI), grounded in land surface ecohydrological processes (Berg and McColl, 2021), was employed. The EI is defined as

$$\mathrm{EI} = \mathrm{LAI} - (\mathrm{a} \times \mathrm{cor}(\mathrm{SM}, \mathrm{Tran}) + \mathrm{b}) \tag{2}$$

where LAI presents the leaf area index, and $\mathrm{cor}(\mathrm{SM}, \mathrm{Tran})$ denotes the correlation between vegetation transpiration (Tran) and soil moisture (SM). Parameters a and b were derived by fitting the relationship $\mathrm{LAI} = (\mathrm{a} \times \mathrm{cor}(\mathrm{SM}, \mathrm{Tran}) + \mathrm{b})$ along $\mathrm{AI} = 0.65$ contour line, marking the transition between aridity and non-aridity climatic conditions. By design, drylands (areas where $\mathrm{AI} < 0.65$) roughly align with regions where $\mathrm{EI} < 0$. Lower EI values reflect more severe vegetation water stress (Berg and McColl, 2021). Since the calculation of EI relies on the correlation between SM and Tran, we applied a 15-year moving window to compute cor(SM,Tran) and mean LAI. The seasonal time lag effect of climatic aridity on the ecohydrological aridity can be ignored in our analysis because the EI value was calculated during a 15-year period, which represents long-term mean ecohydrological aridity conditions.

2.2. Data for estimating AI and EI

Annual precipitation and potential evapotranspiration were used to compute AI. We employed four widely used global precipitation datasets: the Climatic Research Unit gridded Time Series (CUR TS v4.07) dataset (Harris et al., 2020), Global Precipitation Climatology Centre (GPCC) v2020 precipitation product (Becker et al., 2013), Climate Prediction Center (CPC) dataset (Chen et al., 2008), and Multi-Source Weighted-Ensemble Precipitation (MSWEP) product (Beck et al., 2019). For PET, we employed four datasets, including the CRU PET product (Harris et al., 2020), Global Land Evaporation Amsterdam Model (GLEAM) v3.5a product (Martens et al., 2017), hourly PET (hPET) product (Singer et al., 2021), and a custom PET dataset estimated using a revised Penman-Monteith method that incorporate variations in stomatal resistance driven by atmospheric CO_2 level, based on the monthly Multi-Source Weather (MSWX) climate product (Beck et al., 2022). Modified Penman-Monteith formulation is as follows (Yang, 2019):

$$PET = \frac{0.408\ s\ R_n + \gamma \frac{900}{T + 273} D\ u}{s + \gamma \left\{1 + u \left[0.34 + 2.4 \times 10^{-4} ([CO_2] - 300)\right]\right\}} \tag{3}$$

where s represents slope vapor pressure curve (Kpa $^{\circ}C^{-1}$); R_n denotes the net radiation (MJ m^{-2} mon^{-1}); T denotes 2-meter air temperature (°C); γ stands for psychrometric constant (Kpa $^{\circ}C^{-1}$); u refers to 2-meter wind speed (m s^{-1}), estimated from estimated from 10-meter wind speed; D represents vapor pressure deficit (KPa); and $[CO_2]$ stands for the atmospheric CO_2 concentration (ppm).

The EI was estimated from LAI, vegetation transpiration, and soil moisture. We used three LAI datasets: the Long-term Global Mapping (GLOBMAP) (Liu et al., 2012), Global Land Surface Satellite (GLASS) (Liang et al., 2021), and Global Inventory Modeling and Mapping Studies (GIMMS) (Cao et al., 2023) LAI datasets. Three soil moisture products, including ERA5-Land (Muñoz-Sabater et al., 2021), GLEAM (Martens et al., 2017) and CPC (Fan and van den Dool, 2004), were used. Two vegetation transpiration datasets were employed: GLEAM and ERA5-Land products. All data were resampled to 0.5° for final analyses. Table 1 shows the details of the used datasets.

Table 1
Details and sources of the used datasets.

Variable	Data	Spatial Resolution	Temporal Resolution	Data source
LAI	GIMMS LAI	1/12°	bi-weekly	GIMMS[1]
	GLASS LAI	1/12°	bi-weekly	GLASS[2]
	GLOBMAP LAI	1/12°	bi-weekly/ 8-day	GLOBMAP[3]
Transpiration	GLEAM transpiration	0.25°	annual	GLEAM v3.7a[4]
	ERA5-Land transpiration	0.1°	monthly	ERA5-Land[5]
Soil moisture	CPC SM	0.5°	daily	CPC SM[6]
	ERA5-Land SM	0.1°	monthly	ERA5-Land[5]
	GLEAM SM	0.25°	monthly	GLEAM v3.7a[4]
Precipitation	CPC precipitation	0.5°	daily	CPC[7]
	CRU precipitation	0.5°	monthly	CRU TS4.07[8]
	GPCC precipitation	0.5°	monthly	GPCC v2022[9]
	MSWEP precipitation	0.1°	daily/ monthly	MSWEP[10]
PET	CRU PET	0.5°	monthly	CRU TS4.07[8]
	GLEAM PET	0.25°	monthly	GLEAM v3.7a[4]
	hPET PET	0.05°	6-hour	hPET[11]
	MSWX-derived PET	0.1°	monthly	MSWX[12]
GPP	GLASS GPP	0.05°	8-day	GLASS[2]
	NIRv GPP	0.05°	monthly	NIRv[13]
	MUSES GPP	0.05°	8-day	MUSES[14]
	BESS GPP	0.05°	monthly	BESS v2[15]
Evapotranspiration	GLEAM ET	0.25°	annual	GLEAM v3.7a[4]
	ERA5-Land ET	0.1°	monthly	ERA5-Land[5]
Climate variables	air temperature	0.1°	monthly	MSWX[12]
	air pressure	0.1°	monthly	MSWX[12]
	relative humidity	0.1°	monthly	MSWX[12]
Atmospheric CO_2 concentration	CO_2 concentration	Globally averaged	monthly	NOAA/ GML[16]
Biotic data	Dryland regions	–	–	Bailey (1995)
	Land use/ cover	0.01°	annual	HILDA+[17]

2.3. *Canopy stomatal conductance (g_s) and water use efficiency (WUE)*

We assessed eCO_2-related physiological characteristics, specifically canopy g_s and WUE. The estimation of canopy g_s was approximately by delineating the vapor pressure difference with atmospheric vapor pressure deficit (VPD), assuming that leaf and atmosphere temperatures were equal, and ignoring aerodynamic resistance within the boundary layer (Beer et al., 2009). The canopy g_s was calculated as:

$$g_s \approx Tran \times P_a / (1.6 \times VPD) \tag{4}$$

We also replaced vegetation transpiration with evapotranspiration, as previous studies have done (Beer et al., 2009), as described below:

$$g_s \approx ET \times P_a / (1.6 \times VPD) \tag{5}$$

where Tran and ET represent the vegetation transpiration and actual evapotranspiration (ET) (mm), respectively, using GLEAM and ERA5-Land products; Pa denotes atmospheric pressure (kPa), using the MSWX climate product; VPD indicates vapor pressure deficit (kPa); and factor 1.6 indicates the higher diffusion rate of H_2O molecules compared to CO_2. Finally, we obtained 4 (2 ET + 2 transpiration) ensemble members of canopy g_s.

WUE was determined as the ratio of gross primary productivity (GPP) to evapotranspiration (ET), or alternatively, vegetation transpiration (Li et al., 2023b). We used four global GPP datasets: GLASS product (Yuan et al., 2010), Breathing Earth System Simulator (BESS) GPP (Li et al., 2023a), NIRv-derived GPP (Wang et al., 2021b), and Multiscale Satellite Remote Sensing (MUSES) GPP (Wang et al., 2021a). ET and transpiration in GLEAM and ERA5-Land products were used. Finally, we had 16 (4 GPP × 4 ET/transpiration) ensemble members of WUE.

2.4. *Land–atmosphere coupling strength*

We measured land–atmosphere coupling (LAC) strength using a two-legged index, linking the correlations for soil moisture *vs.* land surface evapotranspiration, and land surface evapotranspiration *vs.* precipitation (Dirmeyer, 2011).

$$LAC = R_{SM\_ET} \times R_{ET\_P} \times \sigma_P \tag{6}$$

where R_{SM_ET} and R_{ET_P} represent the correlations between soil moisture and evapotranspiration, and between evapotranspiration and precipitation, respectively; σ_P stands for the standard deviation of precipitation. An increase in LAC indicates a strengthening of land–atmosphere coupling. We used four precipitation datasets, three soil moisture datasets, and two evapotranspiration datasets (i.e., GLEAM and ERA5-

---

[1] GIMMS:https://pan.baidu.com/s/1mhK2zTA#list/path=%2F.

[2] GLASS: https://www.glass.umd.edu/LAI/AVHRR/.

[3] GLOBMAP:https://doi.org/10.5281/zenodo.4700264.

[4] GLEAM transpiration and evapotranspiration:https://www.gleam.eu.

[5] ERA5-Land:https://doi.org/10.24381/cds.68d2bb30.

[6] CPC soil moisture:https://psl.noaa.gov/data/gridded/data.cpcsoil.html.

[7] CPC precipitation:https://psl.noaa.gov/data/gridded/data.cpc.globalprecip.html.

[8] CRU TS4.07:https://data.ceda.ac.uk/badc/cru/data/cru_ts/cru_ts_4.07.

[9] GPCC v2022:https://doi.org/10.5676/DWD_GPCC/FD_M_V2022_050.

[10] MSWEP:https://www.gloh2o.org/mswep/.

[11] hPET:https://doi.org/10.5523/bris.qb8ujazzda0s2aykkv0oq0ctp.

[12] MSWX:https://www.gloh2o.org/mswx.

[13] NIRv GPP:https://doi.org/10.6084/m9.figshare.12981977.v2.

[14] MUSES:https://zenodo.org/records/3996814.

[15] BESS v2:https://www.environment.snu.ac.kr/bessv2.

[16] Atmospheric CO_2 concentration:https://gml.noaa.gov/ccgg/trends/gl_data.html.

[17] HILDA+:https://doi.org/10.1594/PANGAEA.921846.

Land products), obtaining 24 (4 × 3 × 2) ensemble members of LAC strength estimates.

2.5. Analyses

To ensure robust estimation of both AI and EI, we utilized multiple climatic and ecohydrological datasets. Specifically, we generated 16 ensemble members of AI (4 precipitation × 4 PET datasets) and 18 ensemble members of EI (3 LAI × 3 soil moisture × 2 transpiration datasets). Least-squares linear regression was applied to estimate temporal trends in AI and EI, and only pixels with significant trends ($P < 0.05$) were retained (He et al., 2023b). Spatial patterns of decoupled aridity changes were identified using trends of ensemble mean AI and EI. Since EI was derived using a 15-year moving window, we computed the mean AI within that window to establish an AI time series before estimating its trends. Regions exhibiting increased climatic aridity but decreased ecohydrological aridity were classified as AI↓ & EI↑, whereas those with decreased climatic aridity but increased ecohydrological aridity were denoted as AI↑ & EI↓ (both at $P < 0.05$). We further quantified the proportions of these two contrasting types using 288 ensemble combinations (16 AI × 18 EI). The boundary of global drylands followed Bailey's four global ecoregion domains (Bailey and Kirtley, 1989). To validate our calendar-year analyses, an additional test using growing-season data was conducted. Growing season was defined as April–October in the extratropical Northern Hemisphere (23°N–90°N), year-round in the tropics (23°S–23°N), and October–April in the extratropical Southern Hemisphere (23°S–90°S) (He et al., 2025).

To explore the mechanisms underlying the two contrasting types, we first examined changes in the four components of the AI and EI formulations: precipitation, PET, LAI, and the correlation between soil moisture and transpiration [cor(SM,Tran)]. We then applied ridge regression to assess the relative importance of atmospheric CO_2 concentration, energy factors (temperature and radiation), and water factors (precipitation, soil moisture, and VPD) in driving EI changes. Ridge regression is a well-established approach for mitigating multicollinearity in multiple regression and has been shown to better reproduce terrestrial biosphere model truth (McDonald, 2009; Wang et al., 2022; He et al., 2024). All variables were standardized to z-scores prior to ridge regression analysis.

Further, we used structural equation modeling (SEM) to quantify the pathways linking EI to climate variables through three mediating factors: LAI, g_s, and LAC. The SEM analysis was applied grid-by-grid, and only cells with non-significant chi-square tests ($P > 0.05$) were retained for computing mean path coefficients (He et al., 2025). We also examined the temporal trends of LAI, g_s, WUE, transpiration, soil moisture, and LAC within the two contrasting aridity types.

In addition, we assessed the associations between the contrasts and land cover changes. Long term HIstoric Land Dynamics Assessment+ (HILDA+) land use (1982–2018) and MODIS MOD44B low-vegetation cover data (2000–2018) were used to quantify land-cover transitions (DiMiceli et al., 2022; Winkler et al., 2021).

3. Results

3.1. Patterns of contrasting climatic and ecohydrological aridity changes

Using ensemble estimates of the climatic aridity index (AI) and the ecohydrological aridity index (EI), we evaluated trends in both indices across global drylands for the period 1982–2018 (see Methods). An increase (decrease) in AI indicates less (more) arid climatic conditions,

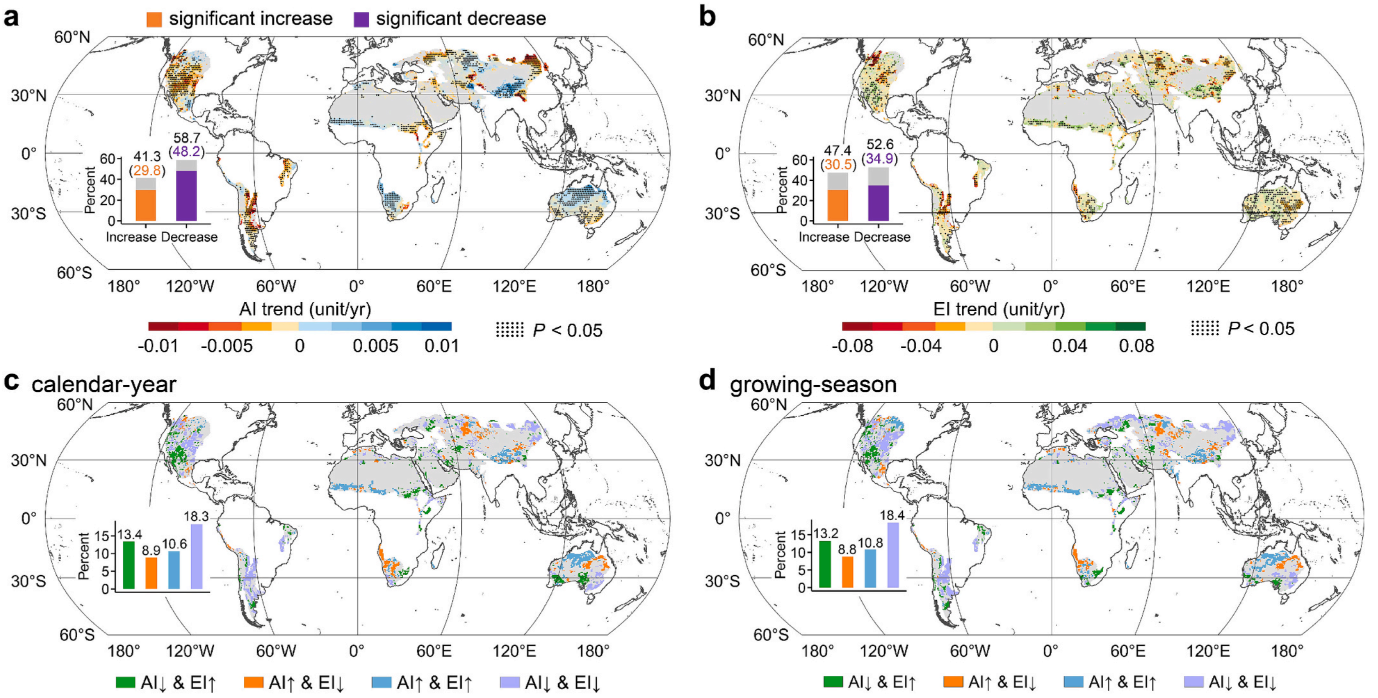

Fig. 1. Patterns of contrasting climatic and ecohydrological aridity changes across drylands during 1982–2018. (a) Trends in the ensemble mean climatic aridity index (AI) estimated from 16 AI members (4precipitation × 4PET datasets). (b) Trends in the ensemble mean ecohydrological aridity index (EI) estimated from 18 EI members (3 LAI × 3 soil moisture × 2 transpiration datasets). Inner subplots in (a) and (b) show the percentage of dryland grid cells with increased and decreased AI and EI, respectively. Gray color indicates the percent of grid cells with non-significant changes. (c, d) Spatial distribution of dryland ecosystems showing four combinations of significant ($P < 0.05$) climatic and ecohydrological aridity changes: (i) increased climatic aridity but decreased ecohydrological aridity (AI↓ & EI↑), (ii) decreased climatic aridity but increased ecohydrological aridity (AI↑ & EI↓), (iii) decreased climatic and ecohydrological aridity (AI↑ & EI↑), and (iv) increased climatic and ecohydrological aridity (AI↓ & EI↓), using calendar-year and growing-season data, respectively. Inner subplots in (c) and (d) show the percentage of dryland area within each category, derived from 288 ensemble combinations (3 LAI × 3 SM × 2 Tran × 4P × 4PET datasets). Gray shading in maps indicates the extent of global drylands.

whereas an increase in EI reflects reduced ecohydrological aridity, meaning greater vegetation growth (higher LAI) and/or lower water limitation. AI significantly increased over 29.8 ± 8.7% (mean ± standard deviation) of global drylands ($P < 0.05$), mainly across southern Africa, Kazakhstan, the Tibetan Plateau, and northern Australia (Fig. 1a). In contrast, AI significantly decreased over 48.2 ± 8.7% of drylands, with notable declines in the western United States, South America, eastern Russia, and the Mongolian Plateau (Fig. 1a). A significant increase in EI occurred in 30.5 ± 3.2% of global drylands ($P < 0.05$), concentrated in the southwestern United States, the southern Sahara, and western Australia (Fig. 1b). Conversely, 34.9 ± 3.4% of drylands showed significant EI decreases, primarily across the central and northwestern United States, South America, Kazakhstan, and eastern Australia (Fig. 1b).

Considering grid cells with significant trends in both AI and EI ($P < 0.05$), 28.9 ± 2.6% of global drylands exhibited consistent climatic and ecohydrological aridity changes. Specifically, 10.6 ± 2.6% showed simultaneous increases and 18.3 ± 4.0% simultaneous decreases in both indices between 1982 and 2018 (Fig. 1c). However, a substantial portion, 22.3 ± 2.5% of global drylands, displayed contrasting aridity changes. Among these, 13.4 ± 2.7% experienced increased climatic aridity but decreased ecohydrological aridity (AI↓ & EI↑), whereas 8.9 ± 3.6% exhibited the opposite trend (AI↑ & EI↓) (Fig. 1c). The AI↓ & EI↑ pattern was concentrated in the western United States and southern Australia, while the AI↑ & EI↓ pattern predominated in Kazakhstan, southern Africa, and northeastern Australia (Fig. 1c). To test the robustness of these results, we repeated the analysis using growing-season data. The spatial distribution of contrasting climatic and ecohydrological aridity changes remained consistent with that derived from the calendar-year analysis (Fig. 1c, d).

3.2. *Mechanisms behind the two contrasting modes*

To identify the potential drivers of climatic and ecohydrological aridity changes, we first examined changes in the four components of the equations used to calculate AI and EI: precipitation, PET, LAI, and the soil moisture–transpiration correlation [cor(SM,Tran)] over the two contrast types during 1982–2018 (Fig. 2).

For climatic aridity, most AI↓ & EI↑ regions experienced a significant decrease in annual precipitation (79.2 ± 6.1%, $P < 0.05$) and an increase in annual PET (92.1 ± 4.7%, $P < 0.05$). In contrast, AI↑ & EI↓ regions showed increases in both precipitation (98.5 ± 1.0%) and PET (69.8 ± 14.4%, $P < 0.05$) (Fig. 2). These patterns indicate that precipitation exerted the dominant control on climatic aridity changes, consistent with the relatively uniform global increase in PET under warming and the stronger spatial heterogeneity of precipitation (Fu and Feng, 2014).

For ecohydrological aridity, most AI↓ & EI↑ regions exhibited significant increases in LAI (57.8 ± 13.4%, $P < 0.05$) and decreases in cor(SM,Tran) (90.5 ± 5.9%, $P < 0.05$), indicating reduced soil moisture limitation on vegetation growth. Conversely, AI↑ & EI↓ regions showed increases in both LAI (70.8 ± 13.2%, $P < 0.05$) and cor(SM,Tran) (98.0 ± 1.7%, $P < 0.05$), implying that vegetation growth became more tightly constrained by soil moisture despite overall wetter climatic conditions. These results highlight the dominant role of soil moisture limitation in shaping the divergent ecohydrological aridity responses between the two contrast types: AI↓ & EI↑ regions became less water-limited, whereas AI↑ & EI↓ regions became more water-limited, despite both experiencing LAI increases.

We next quantified the influence of eCO$_2$, energy factors (temperature and radiation), and water factors (precipitation, soil moisture, and VPD) on EI using ridge regression analysis. Results revealed that eCO$_2$ was the dominant predictor of EI variability, exerting opposite effects between the two contrast types, positive in AI↓ & EI↑ regions and negative in AI↑ & EI↓ regions (Fig. 3). These contrasting effects likely arise through three main pathways: (1) CO$_2$ fertilization enhances vegetation canopy, enhancing transpiration and altering ecosystem water balance (Kergoat et al., 2002); (2) Reduced stomatal conductance (g_s) under eCO$_2$ improves WUE and conserves soil moisture (Gonsamo et al., 2021); (3) CO$_2$-driven shifts in vegetation–atmosphere coupling may amplify or dampen the ecohydrological response to climatic aridity changes (Berg and McColl, 2021). To verify these pathways, we performed SEM analyses linking EI to climatic drivers via three mediating variables—LAI, g_s, and LAC. SEM results confirmed that eCO$_2$ exerted the strongest overall effect on EI among all drivers, mainly through LAI and g_s, while the indirect effect via LAC was comparatively weak (Fig. 4). In AI↓ & EI↑ regions, eCO$_2$ and soil moisture had positive effects on EI mediated by increases in LAI and reductions in g_s (Fig. 4a, c, e). In contrast, in AI↑ & EI↓ regions, eCO$_2$, energy, and water factors exerted negative effects on EI, again primarily via LAI and g_s (Fig. 4b, d, f). The opposing influences of eCO$_2$ and water factors through LAC largely canceled each other, resulting in negligible net LAC effects on EI (Fig. 4a and b).

In AI↓ & EI↑ regions, eCO$_2$ led to a significant decline in g_s (–15.5 ± 7.1 units yr^{-1}) and a rise in WUE (0.010 ± 0.012 g C mm^{-1} yr^{-1}) (Fig. 5a and b). This indicates enhanced water-saving capacity, which reduced transpiration and helped maintain higher LAI (Fig. 5c and d). Overall, the positive physiological effects of eCO$_2$ outweighed the adverse impacts of declining AI and soil moisture (Fig. 4a, c; Fig. 5e). Locally, the greater LAI implies larger self-shading, higher carbon uptake, greater biomass accumulation, and deeper rooting depth, collectively enhancing vegetation resilience to intensified climatic aridity (Kergoat et al., 2002; Gitelson et al., 2014). In contrast, in AI↑ & EI↓ regions, weak eCO$_2$-induced water savings (g_s trend: 1.7 ± 6.8 units yr^{-1}; WUE trend: 0.003 ± 0.012 g C mm^{-1} yr^{-1}) coupled with enhanced vegetation structure (increased LAI) led to increased transpiration (Fig. 5c, d), likely surpassing the ecosystems' water-supply capacity (Jump et al., 2017; Li

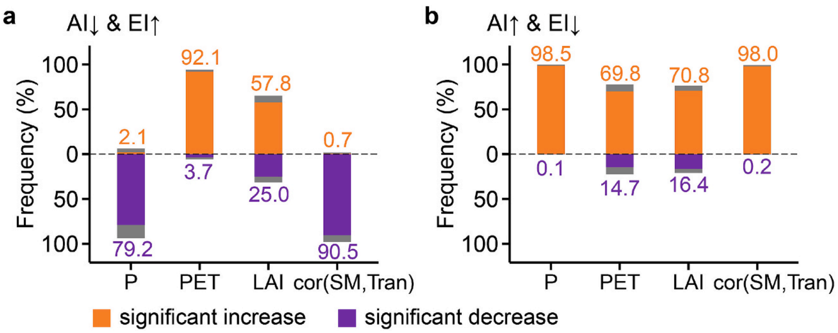

Fig. 2. Changes in the four components used to calculate AI and EI. (a) Fractions of grid cells showing significant ($P < 0.05$) increasing or decreasing trends in annual precipitation (P), potential evapotranspiration (PET), leaf area index (LAI), and the correlation between soil moisture and transpiration [cor(SM,Tran)] in AI↓ & EI↑ regions. (b) Same as (a), but for AI↑ & EI↓ regions. Gray bars indicate non-significant trends.

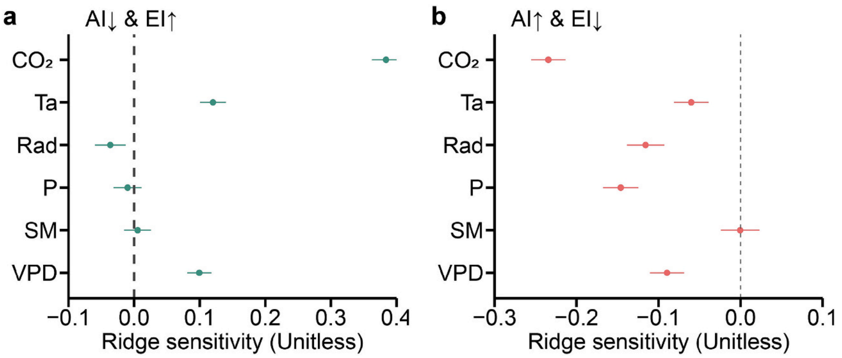

Fig. 3. Ridge regression sensitivities of climatic factors to EI changes for the two contrast types. (a and b) Results for AI↓ & EI↑ and AI↑ & EI↓ regions, respectively. CO_2, Ta, Rad, P, SM, and VPD indicate atmosphere CO_2 concentration, air temperature, radiation, precipitation, soil moisture and vapor pressure deficit, respectively. Bars denote standard errors.

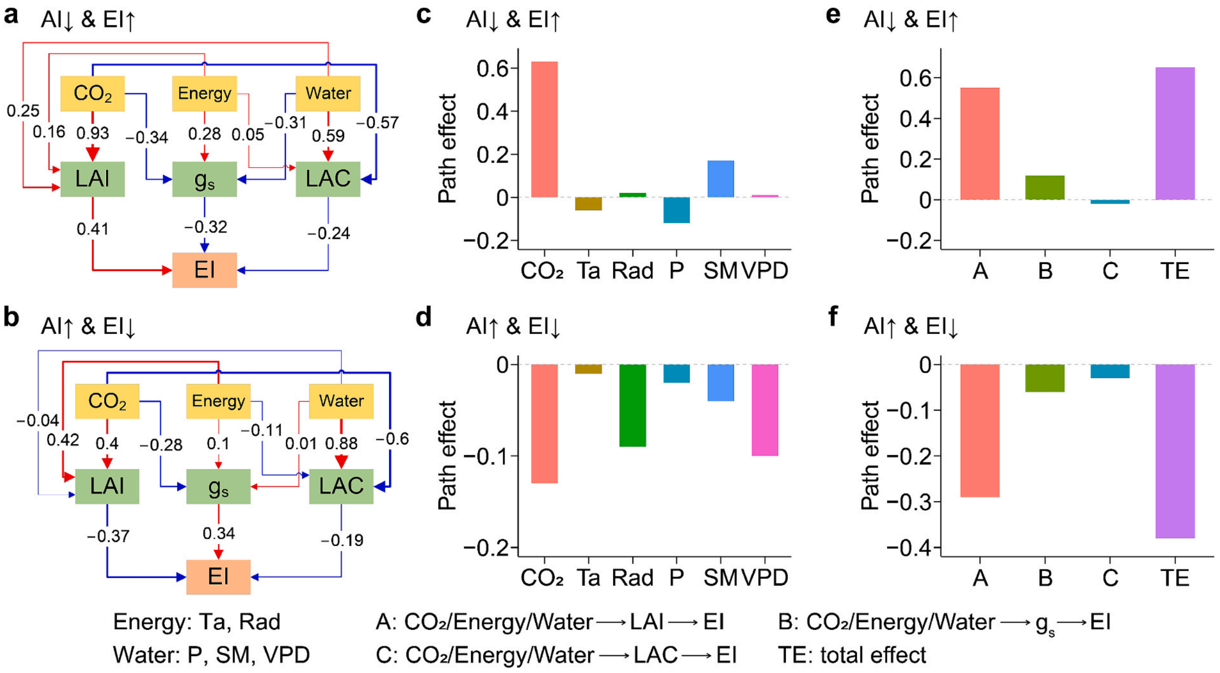

Fig. 4. Structural equation models (SEMs) describing drivers and mediating pathways of EI changes. (a and b) SEM pathways for AI↓ & EI↑ and AI↑ & EI↓ regions, respectively. (c and d) Total effects of individual climate factors on EI in the two contrast types. CO_2, Ta, Rad, P, SM, and VPD indicate atmosphere CO_2 concentration, air temperature, radiation, precipitation, soil moisture and vapor pressure deficit, respectively. Energy factors include Ta and Rad; water factors include P, SM, and VPD. (e and f) Total effects of mediating variables—leaf area index (LAI), stomatal conductance (g_s), and land–atmosphere coupling strength (LAC)—on EI in the two contrast types.

et al., 2023c; Zhang et al., 2025). Consequently, these regions experienced greater plant water stress and enhanced ecohydrological aridity, even as climatic aridity lessened. Although the overall influence of LAC on EI was weak, the strengthening of land–atmosphere coupling (increased LAC) in AI↑ & EI↓ regions may further amplify vegetation water stress by enhancing transpiration, thereby reinforcing ecohydrological aridity even under wetter climatic conditions (Figs. 4b, f, 5c, f).

Finally, we examined whether the observed divergent changes in aridity could be attributed to recent land cover changes. Our analysis revealed that land cover transitions accounted for only a small fraction of regions with contrasting aridity changes (1.2% for AI↓ & EI↑ and 0.7% for AI↑ & EI↓), with a similarly limited contribution from croplands (1.5% *vs.* 0.4%) (Fig. 6). Moreover, since most contrasting ecosystems (~90%) were low-vegetation biomes (i.e., grasslands and shrublands), we further examined changes in low-vegetation cover. Both contrast types exhibited comparable magnitudes of increase or decrease in low-vegetation cover during 2000–2018, with no consistent directional trend (Fig. 7). These findings suggest that the two contrasting aridity modes were not primarily driven by land cover change.

4. Discussion

Our study reveals that approximately one-fifth of global drylands have exhibited a decoupling between climatic and ecohydrological aridity over the past four decades. These divergent changes indicate that vegetation responses are not necessarily synchronized with climatic variability, giving rise to nonlinear ecosystem dynamics that complicate projections of global carbon–water interactions (Sasaki et al., 2023; He et al., 2023a; Li et al., 2025). In such regions, future shifts in ecosystem functioning cannot be reliably inferred from projected climatic aridity alone (Berdugo et al., 2020).

Existing research primarily focused on sub-tropical dryland, examining climatic, hydrological, and ecological aridity changes (Shi et al., 2023; Abel et al., 2023; Lian et al., 2021), with some noting

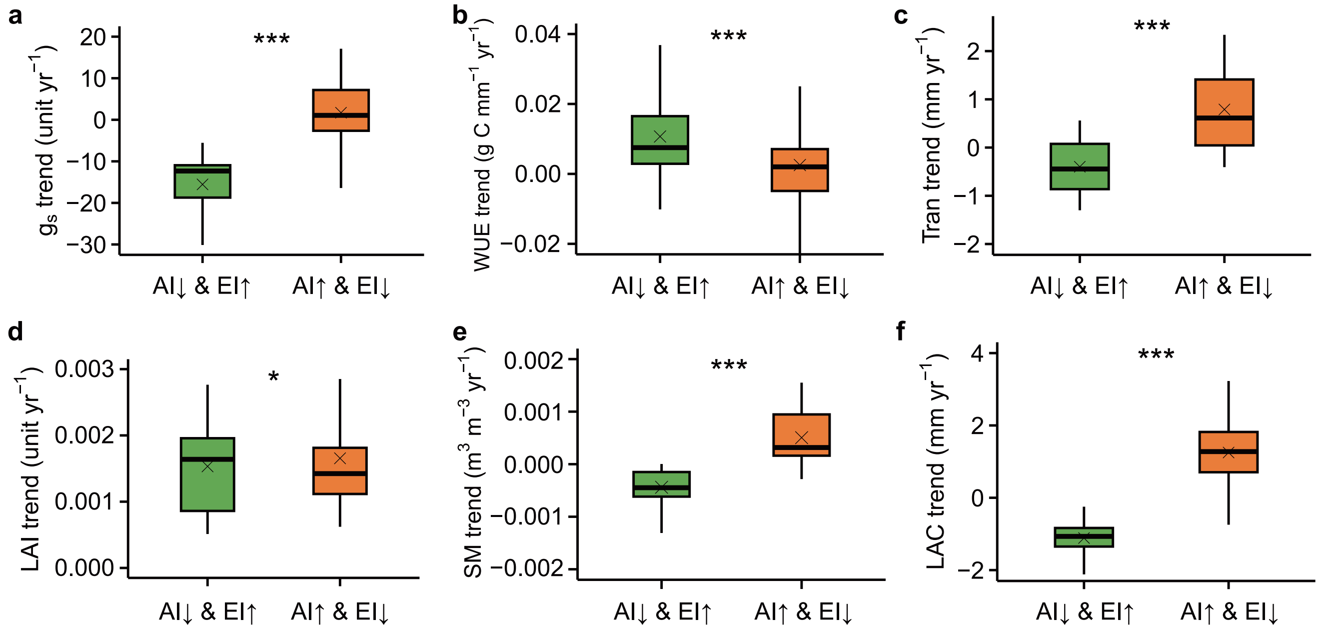

Fig. 5. Trends in ecological, physiological, and hydrological variables in regions with contrasting aridity changes. (a–f) Trends in canopy stomatal conductance (g_s), water use efficiency (WUE), vegetation transpiration (Tran), leaf area index (LAI), soil moisture (SM) and land–atmosphere coupling strength (LAC) in AI↓ & EI↑ and AI↑ & EI↓ regions, respectively.

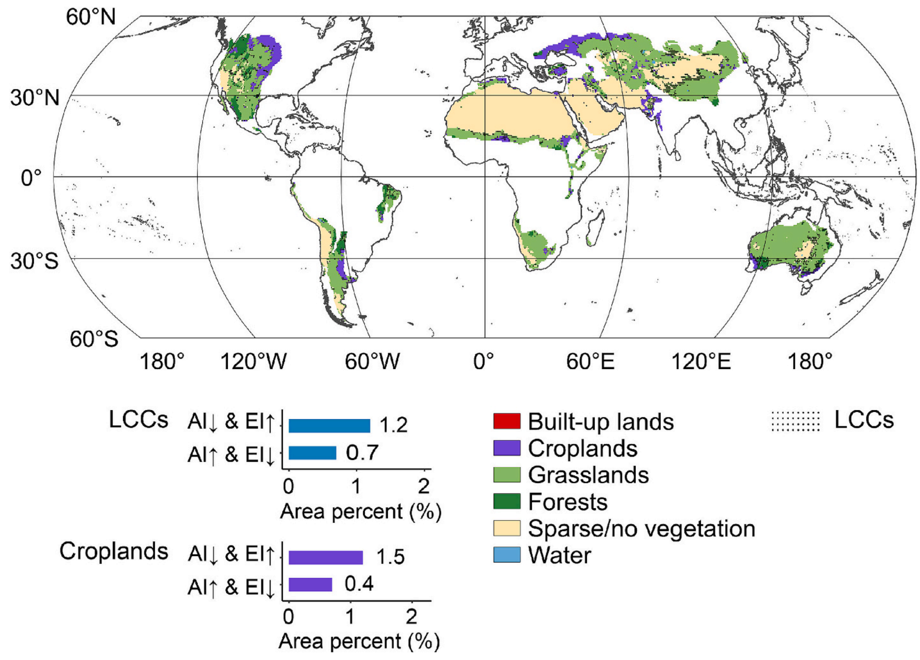

Fig. 6. Land cover (2018) and land cover changes (LCCs) from 1982 to 2018. Inner subplots show percent of areas with contrasting aridity changes in LCCs and croplands.

discrepancies between climatic and ecohydrological aridity changes, especially the AI↓ & EI↑ contrasts (Lian et al., 2021), yet lacking spatial pattern quantification. Our analyses reveal two distinct and contrasting modes of aridity change across global drylands (Fig. 8): increased climatic aridity but decreased ecohydrological aridity (AI↓ & EI↑), and decreased climatic aridity but increased ecohydrological aridity (AI↑ & EI↓), each reflecting fundamentally different ecological pathways. Regions showing AI↓ & EI↑ exhibit enhanced vegetation growth and reduced soil water stress despite increasingly arid climatic conditions, suggesting that ecosystems possess a buffering capacity against climatic drying. In contrast, AI↑ & EI↓ regions experience intensified vegetation water limitation even under a climatically wetter environment, indicating that increased atmospheric moisture does not necessarily translate into improved ecohydrological conditions. These decoupling aridity changes reveal that ecosystems respond to climatic aridity in a nonlinear and internally regulated manner (Long et al., 2025), underscoring that ecohydrological processes play a central role in determining resilience under future climate change.

Mechanistically, the decoupling between climatic and ecohydrological aridity likely arises from oppositive effects of eCO_2 on EI through

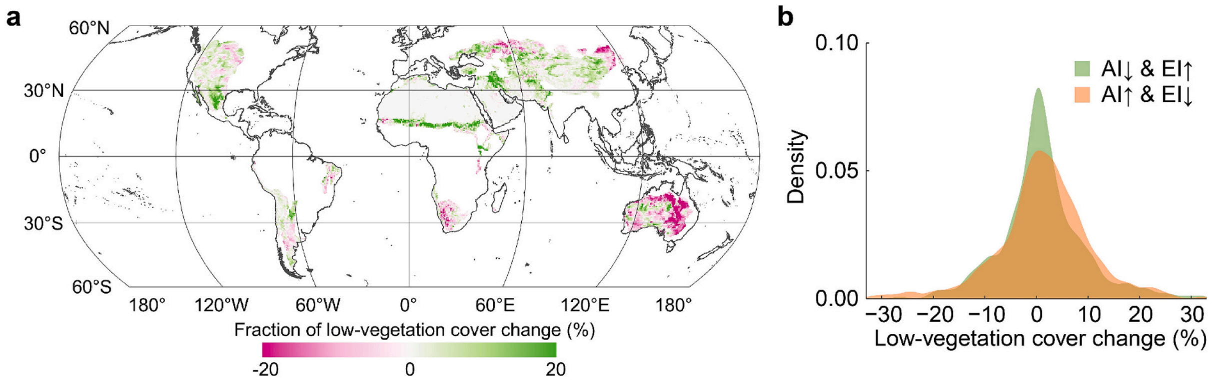

Fig. 7. Changes in low-vegetation cover during 2000–2018. (a) Fractional changes in low-vegetation cover. (b) Density distribution of low-vegetation cover change in the two contrast types (AI↓ & EI↑ and AI↑ & EI↓).

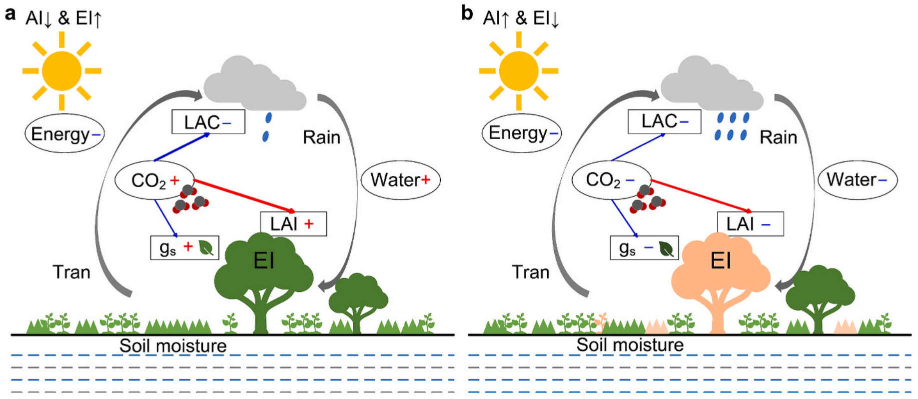

Fig. 8. Conceptual schematic illustrating decoupling between climatic and ecohydrological aridity changes. (a) The contrasting mode of increased climatic aridity but decreased ecohydrological aridity (AI↓ & EI↑). (b) The opposite mode—decreased climatic aridity but increased ecohydrological aridity (AI↑ & EI↓). Plus (+) and minus (–) signs indicate positive or negative effects on EI, respectively.

changes in vegetation structure (leaf area) and physiology (canopy g_s) (Fig. 8). The eCO_2-induced reduction in canopy g_s and enhancement of WUE decrease transpiration, improve water conservation, and stimulate vegetation growth, thereby offsetting the impacts of increased climatic aridity in AI↓ & EI↑ regions (Rifai et al., 2022; Gonsamo et al., 2021). When the vegetation's water-saving capacity has not yet reached saturation, increased LAI can enhance self-shading, carbon assimilation, and belowground biomass accumulation (i.e., deeper rooting), collectively strengthening ecosystem resilience to climatic drying. Conversely, AI↑ & EI↓ regions exhibit minimal changes in canopy g_s and only modest WUE increases, implying weak eCO_2-induced water savings. Combined with increased vegetation structural investment (e.g., higher LAI), such regions may exceed their ecohydrological carrying capacity (Jump et al., 2017), intensifying transpiration and water stress and leading to ecohydrological drying. Moreover, stronger land–atmosphere coupling can enhance vegetation transpiration, further contributing to ecohydrological drying in AI↑ & EI↓ regions. Looking ahead, the persistence or expansion of AI↑ & EI↓ regions may be amplified by WUE saturation under elevated VPD and intensified land–atmosphere coupling that promotes evaporative loss (Li et al., 2023b; Koppa et al., 2024). Collectively, these processes may enhance ecohydrological aridity and weaken the terrestrial carbon sink under a future warming climate.

In this study, we calculated the ecohydrological aridity index (EI) based on the relationship between vegetation growth (structural state) and soil moisture limitation, expressed as the correlation between soil moisture and transpiration [cor(SM,Tran)] within a 15-year moving window (Berg and McColl, 2021). This method captures the long-term mean ecohydrological state and is appropriate for assessing multi-decadal ecohydrological aridity dynamics such as those examined here. However, using a long-term moving window inevitably smooths short-term and interannual fluctuations in soil moisture–vegetation interactions, potentially obscuring transient ecohydrological responses. This limitation underscores the need to develop annual or sub-annual ecohydrological aridity indices capable of capturing rapid changes, particularly during ecological drought events. Future efforts could integrate ecosystem water demand (Cui et al., 2024) with high-temporal-resolution (e.g., daily) soil moisture and transpiration datasets to achieve this goal.

5. Conclusion

We show that changes in plant dynamics do not reflect changes in climate aridity in 22.3% of global drylands. Divergent changes in climatic and ecohydrological aridity changes mean that climate cannot adequately predict vegetation dynamics across these regions, complicating future biochemical predictions. Our study analyzes the spatial patterns and mechanisms of the decoupling between climatic aridity changes and ecological responses, thus informing our understanding of vegetation acclimation and adaptation in a warming climate. During our studied period, 13.4% of global drylands experienced increased climatic aridity at the same time with decreased ecohydrological aridity (AI↓ & EI↑), while 8.9% exhibited the opposite trend (AI↑ & EI↓). These two contrasting modes were primarily driven by opposite eCO_2 effects on vegetation structure (leaf area index) and physiology (canopy stomatal conductance). In AI↓ & EI↑ regions, strong eCO_2-induced water conservation and vegetation greening mitigated the effects of climatic drying, while in AI↑ & EI↓ regions, limited eCO_2 benefits, increased vegetation water demand, and stronger land–atmosphere feedbacks intensified ecohydrological stress. Our findings highlight, quantify and analyze the processes underlying observed regional divergences in contrasting climatic and ecohydrological aridity changes over drylands. These divergences offer an important benchmark for evaluating and refining Earth system models, and eventually contributing to more reliable projections of the carbon cycle and climate dynamics.

CRediT authorship contribution statement

Lei He: Writing – original draft, Software, Methodology, Formal analysis, Data curation, Conceptualization. **Alexis Berg:** Writing – review & editing, Methodology, Formal analysis. **Kailiang Yu:** Writing – review & editing, Formal analysis. **Jian-Sheng Ye:** Writing – review & editing, Methodology, Investigation, Formal analysis. **Josep Peñuelas:** Writing – review & editing, Investigation, Formal analysis. **Philippe Ciais:** Writing – review & editing, Investigation, Formal analysis. **Jingfeng Xiao:** Writing – review & editing, Methodology, Investigation, Formal analysis. **Xu Lian:** Writing – review & editing, Formal analysis. **Jianping Huang:** Writing – review & editing, Investigation, Formal analysis. **Jing Li:** Writing – review & editing, Methodology. **Wei Li:** Writing – review & editing, Formal analysis. **Jian Peng:** Writing – review & editing, Investigation, Formal analysis. **Songhan Wang:** Writing – review & editing, Formal analysis. **Ning Ma:** Writing – review & editing, Formal analysis. **Zecheng Guo:** Writing – review & editing, Visualization, Formal analysis. **Thomas W. Crowther:** Writing – review & editing, Investigation, Formal analysis. **Jiangpeng Cui:** Writing – review & editing, Formal analysis. **Chenghu Zhou:** Writing – review & editing, Investigation. **Yaowen Xie:** Writing – review & editing, Formal analysis, Conceptualization. **Zhao-Liang Li:** Writing – review & editing, Validation, Investigation, Formal analysis, Conceptualization.

Declaration of competing interest

The authors declare that they have no known competing financial interests or personal relationships that could have appeared to influence the work reported in this paper.

Acknowledgments

This work was funded by the National Natural Science Foundation of China (41921001) and the Data Intelligence Laboratory of Tibetan Plateau Humanistic Environment (Lanzhou University). We thank Dr. Kaighin A. McColl and Dr. Yao Zhang for their valuable comments on the initial manuscript.

Data availability

All used datasets are openly accessible, with their sources detailed in Table 1.

The codes are available on Zenodo (https://doi.org/10.5281/zenodo.14264828).

References

Abel, C., et al., 2023. Contrasting ecosystem vegetation response in global drylands under drying and wetting conditions. Glob. Chang. Biol., gcb.16745

Bailey, R.G. and Kirtley, M. 1989. Ecoregions of the continents.

Becker, A., et al., 2013. A description of the global land-surface precipitation data products of the global precipitation climatology centre with sample applications including centennial (trend) analysis from 1901–present. Earth Syst. Sci. Data 5, 71–99.

Beck, H.E., et al., 2019. MSWEP V2 global 3-hourly 0.1° precipitation: methodology and quantitative assessment. Bull. Am. Meteorol. Soc. 100, 473–500.

Beck, H.E., et al., 2022. MSWX: global 3-hourly 0.1° bias-corrected meteorological data including near-real-time updates and forecast ensembles. Bull. Am. Meteorol. Soc. 103, E710–E732.

Beer, C., et al., 2009. Temporal and among-site variability of inherent water use efficiency at the ecosystem level. Glob. Biogeochem. Cycles. 23, 2008GB003233.

Berdugo, M., et al., 2020. Global ecosystem thresholds driven by aridity. Science 367, 787–790.

Berg, A., McColl, K.A., 2021. No projected global drylands expansion under greenhouse warming. Nat. Clim. Change 11, 331–337.

Cao, S., et al., 2023. Spatiotemporally consistent global dataset of the GIMMS leaf area index (GIMMS LAI4g) from 1982 to 2020. Earth Syst. Sci. Data 15, 4877–4899.

Chai, Y., et al., 2025. Underestimating global land greening: Future vegetation changes and their impacts on terrestrial water loss. One Earth 8.

Chen, M., et al., 2008. Assessing objective techniques for gauge-based analyses of global daily precipitation. J. Geophys. Res. Atmos. 113, 2007JD009132.

Chou, C., et al., 2009. Evaluating the "rich-get-richer" mechanism in tropical precipitation change under global warming. J. Clim. 22, 1982–2005.

Cook, B.I., et al., 2014. Global warming and 21st century drying. Clim. Dyn. 43, 2607–2627.

Cui, J., et al., 2024. Integrating ecosystem water demands into drought monitoring and assessment under climate change. Nat. Water 2, 215–218.

Dai, A., et al., 2018. Climate change and drought: a precipitation and evaporation perspective. Curr. Clim. Change Rep. 4, 301–312.

DiMiceli, C., et al. 2022. MOD44B MODIS/Terra Vegetation Continuous Fields Yearly L3 Global 250m SIN Grid V006.

Dirmeyer, P.A., 2011. The terrestrial segment of soil moisture-climate coupling. Geophys. Res. Lett. 38.

Donohue, R.J., et al., 2013. Impact of CO_2 fertilization on maximum foliage cover across the globe's warm, arid environments. Geophys. Res. Lett. 40, 3031–3035.

Fan, Y., van den Dool, H., 2004. Climate Prediction Center global monthly soil moisture data set at 0.5° resolution for 1948 to present. J. Geophys. Res. Atmos. 109.

Fu, Q., Feng, S., 2014. Responses of terrestrial aridity to global warming. J. Geophys. Res. Atmos. 119, 7863–7875.

Gitelson, A.A., et al., 2014. Relationships between gross primary production, green LAI, and canopy chlorophyll content in maize: Implications for remote sensing of primary production. Remote Sens. Environ. 144, 65–72.

Gonsamo, A., et al., 2021. Greening drylands despite warming consistent with carbon dioxide fertilization effect. Glob. Chang. Biol. 27, 3336–3349.

Harris, I., et al., 2020. Version 4 of the CRU TS monthly high-resolution gridded multivariate climate dataset. Sci. Data 7, 109.

He, L., et al., 2023a. Non-symmetric responses of leaf onset date to natural warming and cooling in northern ecosystems. PNAS Nexus 2, pgad308.

He, L., et al., 2023b. Precipitation regimes primarily drive the carbon uptake in the Tibetan Plateau. Ecol. Ind. 154, 110694.

He, L., et al., 2024. Asymmetric temperature effect on leaf senescence and its control on ecosystem productivity. PNAS Nexus 3, pgae477.

He, L., et al., 2025. Lagged precipitation effects on plant production across terrestrial biomes. Nat. Ecol. Evol. 9, 1800–1811.

Held, I.M., Soden, B.J., 2006. Robust responses of the hydrological cycle to global warming. J. Clim. 19, 5686–5699.

Huang, J., et al., 2016. Accelerated dryland expansion under climate change. Nat. Clim. Chang. 6, 166–171.

Jump, A.S., et al., 2017. Structural overshoot of tree growth with climate variability and the global spectrum of drought-induced forest dieback. Glob. Chang. Biol. 23, 3742–3757.

Kergoat, L., et al., 2002. Impact of doubled CO_2 on global-scale leaf area index and evapotranspiration: conflicting stomatal conductance and LAI responses. J. Geophys. Res. Atmos. 107, ACL 30-1–ACL 30-16.

Koppa, A., et al., 2024. Dryland self-expansion enabled by land–atmosphere feedbacks. Science 385, 967–972.

Lian, X., et al., 2021. Multifaceted characteristics of dryland aridity changes in a warming world. Nat. Rev. Earth Environ. 2, 232–250.

Liang, S., et al., 2021. The global land surface satellite (GLASS) product suite. Bull. Am. Meteorol. Soc. 102, E323–E337.

Li, B., et al., 2023a. BESSv2.0: a satellite-based and coupled-process model for quantifying long-term global land–atmosphere fluxes. Remote Sens. Environ. 295, 113696.

Li, F., et al., 2023b. Global water use efficiency saturation due to increased vapor pressure deficit. Science 381, 672–677.

Li, Y., et al., 2023c. Widespread spring phenology effects on drought recovery of Northern Hemisphere ecosystems. Nat. Clim. Change. 13, 182–188.

Li, X., et al., 2025. Large live biomass carbon losses from droughts in the northern temperate ecosystems during 2016-2022. Nat. Commun. 16, 4980.

Liu, Y., et al., 2012. Retrospective retrieval of long-term consistent global leaf area index (1981–2011) from combined AVHRR and MODIS data. J. Geophys. Res. Biogeosci. 117, 2012JG002084.

Long, J., et al., 2025. Reconstruction of drought propagation pathways: a global analysis of multitype propagation chains and nonlinear mechanisms. Glob. Planet Change., 105144

Martens, B., et al., 2017. GLEAM v3: satellite-based land evaporation and root-zone soil moisture. Geosci. Model Dev. 10, 1903–1925.

McDonald, G.C., 2009. Ridge regression. WIREs Comput. Stat. 1, 93–100.

Miller, D.L., et al., 2023. Increased photosynthesis during spring drought in energy-limited ecosystems. Nat. Commun. 14, 7828.

Muñoz-Sabater, J., et al., 2021. ERA5-Land: a state-of-the-art global reanalysis dataset for land applications. Earth Syst. Sci. Data 13, 4349–4383.

Rifai, S.W., et al., 2022. Thirty-eight years of CO_2 fertilization has outpaced growing aridity to drive greening of Australian woody ecosystems. Biogeosciences 19, 491–515.

Sasaki, T., et al., 2023. Dryland sensitivity to climate change and variability using nonlinear dynamics. Proc. Natl. Acad. Sci. 120, e2305050120.

Scheff, J., Frierson, D.M.W., 2014. Scaling potential evapotranspiration with greenhouse warming. J. Clim. 27, 1539–1558.

Seager, R., et al., 2010. Thermodynamic and Dynamic mechanisms for large-scale changes in the hydrological cycle in response to global warming. J. Clim. 23, 4651–4668.

Sherwood, S., Fu, Q., 2014. A drier future? Science 343, 737–739.

Shi, H., et al., 2023. Global dryland aridity changes indicated by atmospheric, hydrological, and vegetation observations at meteorological stations. Hydrol. Earth Syst. Sci. 27, 4551–4562.

Singer, M.B., et al., 2021. Hourly potential evapotranspiration at 0.1° resolution for the global land surface from 1981-present. Sci. Data 8, 224.

Slette, I.J., et al., 2019. How ecologists define drought, and why we should do better. Glob. Chang. Biol. 25, 3193–3200.

Song, Y., et al., 2022. Increased global vegetation productivity despite rising atmospheric dryness over the last two decades. Earths Future 10, e2021EF002634.

Wang, J., et al., 2021a. New global MuSyQ GPP/NPP remote sensing products from 1981 to 2018. IEEE J. Sel. Top. Appl. Earth Obs. Remote Sens. 14, 5596–5612.

Wang, S., et al., 2021b. Tracking the seasonal and inter-annual variations of global gross primary production during last four decades using satellite near-infrared reflectance data. Sci. Total Environ. 755, 142569.

Wang, Z., et al., 2022. Regressions underestimate the direct effect of soil moisture on land carbon sink variability. Glob. Chang. Biol. 28, 7161–7163.

Winkler, K., et al., 2021. Global land use changes are four times greater than previously estimated. Nat. Commun. 12, 2501.

Yang, Y., 2019. Hydrologic implications of vegetation response to elevated CO_2 in climate projections. Nat. Clim. Change. 9.

Yuan, W., et al., 2010. Global estimates of evapotranspiration and gross primary production based on MODIS and global meteorology data. Remote Sens. Environ. 114, 1416–1431.

Zaitchik, B.F., et al., 2023. Wetting and drying trends under climate change. Nat. Water 1, 502–513.

Zhang, W., et al., 2025. Seasonal stabilization effects slowed the greening of the Northern Hemisphere over the last two decades. Nat. Commun. 16, 6287.

Zhu, Z., et al., 2016. Greening of the earth and its drivers. Nat. Clim. Chang. 6, 791–795.